International Journal of Fatigue 177 (2023) 107922

Contents lists available at ScienceDirect

International Journal of Fatigue

journal homepage: www.elsevier.com/locate/ijfatigue

Experimental and numerical study on the fatigue behaviour of the shot-earth 772

Giovanni Pio Pucillo [a], Andrea Carpinteri [b], Camilla Ronchei [b], Daniela Scorza [b], Andrea Zanichelli [b], Sabrina Vantadori [b,*]

[a] Department of Industrial Engineering, University of Naples Federico II, P.le Tecchio 80, 80125 Naples, Italy
[b] Department of Engineering & Architecture, University of Parma, Parco Area delle Scienze 181/A, 43124 Parma, Italy

ARTICLE INFO

Keywords:
Cyclic tests
Fatigue behaviour
Micromechanical numerical model
Shot-earth
S-N curves

ABSTRACT

The present research work is devoted to the mechanical, fracture and fatigue experimental characterization of the shot-earth 772, with a particular attention to its fatigue behaviour. To such an aim, an extensive experimental program has been carried out, consisting of: (i) flexural and compression tests, (ii) three-point bending fracture tests, and (iii) bending and compression cyclic tests. Moreover, a FE numerical model is employed to simulate both the above bending and compression cyclic tests, after the input data validation performed by simulating the above fracture tests. The numerical fatigue lifetimes are compared with the corresponding experimental ones for both pulsating bending and compression, highlighting the model accuracy. Finally, the contours of both the damage parameter and the reduced Young modulus are plotted showing the evolution of fatigue damage.

1. Introduction

Nowadays many researchers are increasingly devoting to discover and characterise innovative materials able to reduce the environmental impact on energy-consuming and polluting sectors. Among them, the construction industry is one of the main sectors of the world economy, and is responsible for huge energy absorption, environmental pollution and consumption of raw materials, due to the production and transportation of the building materials (the cementitious materials standing out among them) [1]. In such a context, the recent literature mainly focuses on cementitious composites, incorporating different types of unconventional aggregates, filler or reinforcing phases [2]. In particular, different attempts have been made in order to obtain composite materials characterised by: (i) improved physical, mechanical, and fracture/fatigue properties, thus allowing to reduce the amount of materials to be employed and, consequently, alleviating the pollution related to both production and transportation [3–8]; (ii) increased service life and durability of the material, in order to both reduce maintenance operations and postpone substitutions of structural components [9–13].

In such a context, the incorporation of soil in the matrix of cementitious composites is widely employed in order to both improve the physical performance (i.e., thermal and acoustic insulation) of the material and reduce its environmental impact [14]. As far as civil constructions are concerned, different types of earthen construction techniques can be mentioned, such as: poured earth, adobe, superadobe, wattle and daub, rammed earth, cob, and compressed stabilised earth blocks [15–23]. As a matter of fact, earthen materials, based on the use/reuse of excavated soil in the construction industry, offer [21]:

- environmental and ecological benefits, that is, their use allows to reduce CO_2 emissions related to production and long-distance transport, to avoid filling landfills, and to limit the extraction of mined natural resources;
- economic benefits, that is, their use promotes the reduction of costs associated with transportation and disposal;
- benefits in terms of living comfort, that is, their use makes it possible to build civil structures with excellent thermal properties, high indoor-humidity regulation and absent/quasi-zero toxicity levels.

However, despite the above advantages, earthen construction materials are in general characterised by worse mechanical, fracture and fatigue properties with respect to traditional cementitious materials [24]. Therefore, in order to promote the use of such materials, a deep characterisation in terms of mechanical, fracture and fatigue behaviour is needed.

As far as the mechanical properties are concerned, Han et al. [25]

* Corresponding author.
E-mail address: sabrina.vantadori@unipr.it (S. Vantadori).

https://doi.org/10.1016/j.ijfatigue.2023.107922
Received 29 June 2023; Received in revised form 4 August 2023; Accepted 28 August 2023
Available online 29 August 2023

studied the compression properties of both unreinforced and polymer fibre reinforced adobe masonry. An increase of 56% in terms of compressive strength was found for the reinforced adobe with respect to the reference one, and it was observed that the presence of fibres reduced the nucleation and propagation of cracks. In the research work by Kaluder et al. [26], specimens reproducing portions of existing traditional rammed earth buildings were tested in order to determine the shear strength. In particular, small differences in terms of shear strength were observed when different particle size distributions and lime contents were employed, whereas a significant increase was obtained when natural fibres were added to the composites. Moreover, a comparison in terms of both compression and shear properties between adobe, rammed earth and cob was performed in Ref. [27]. During the compression tests, the Authors found that adobe masonry and rammed earth elements were characterised by a brittle behaviour, whereas a more ductile behaviour was observed for cob specimens. Cob specimens also exhibited better shear strength than that of the other materials analysed.

As far as the fracture behaviour is concerned, a limited number of studies is available in the literature. For instance, Arto et al. [28] analysed the fracture behaviour of rammed earth specimens characterised by two different soil–lime ratios, and stated that rammed earth could be considered as a quasi-brittle material following the Hillerborg's crack model. Moreover, Hussaini and Toufigh [29] investigated the fracture properties of rammed earth stabilised with different contents of either cement or pozzolan, and reinforced by glass fibres used in different percentages. When cement or pozzolan were employed, an increased peak load was achieved in the fracture tests, whereas the use of glass fibres promoted a significant load bearing capacity in the post-peak stage. Aymerich et al. [30] investigated the enhancement, in terms of crack resistance, energy absorption and load bearing capacity, provided by the addition of hemp fibres (two fibre contents and three fibre lengths were analysed) into an earthen matrix. The Authors observed that the incorporation of fibres significantly improved the peak load and the fracture energy, as well as the load bearing capacity even at large deformations, by increasing the fibre content and, for the same fibre content, by increasing the fibre length.

As far as the behaviour under cyclic loading is concerned, the research work by Hračov et al. [31] is one of the few available in the literature. In particular, the Authors focused on the influence of two strengthening techniques (X-shaped steel wire ropes or a geo-net, both applied on the specimen surface) on the structural response of both unfired clay and adobe, subjected to a constant vertical compression and a cyclic horizontal displacement. It was observed that the earthen masonry was able to bear higher deformations than the unfired clay bricks. Moreover, the application of both strengthening techniques resulted in an increase of maximum load and of maximum deformation (that the reinforced specimens could withstand) with respect to the unreinforced ones. Further, some Researchers have studied the structural behaviour of rammed earth walls subjected to cyclic loading. Arslan et al. [32], for instance, experimentally investigated the structural behaviour of rammed earth walls subjected to in-plane horizontal cyclic displacements, and observed the best performance in terms of load bearing capacity and dissipated energy when the rammed earth wall was stabilized by 10% of cement. Yang et al. [33] found out that the cyclic behaviour of a cement-stabilised rammed earth wall could be further improved by confining it with steel tie-column elements, thus obtaining higher strength and more ductility.

Among the earthen construction techniques, an innovative one is that named shot-earth technique [34]. In more detail, the material obtained (shot-earth) is composed by a mixture of excavated soil (that may be either unstabilised or stabilised by a chemical binder), aggregates and water. According to such a technique, the dry mixture is blown at high velocity into a spraying hose, and high pressure water is added directly to the spraying nozzle. The material obtained is compacted by the impact on the surface of the support. The applications of the shot-earth

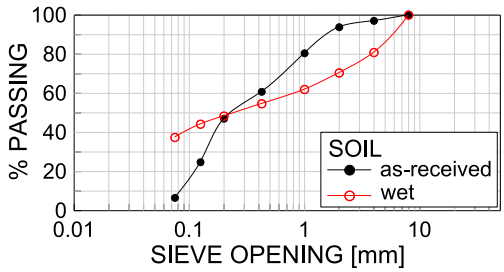

Fig. 1. Cumulative particle-size distribution curves of the soil: as-received and wet.

are those typical of a dry shotcrete, and mainly consist in: new structures, repairs and rehabilitations, and slope and surface protection [35]. However, few works have so far analysed the mechanical and fracture properties of this innovative material [36–39], and none has even investigated its fatigue behaviour.

Therefore, the present research work deals with the experimental characterisation, in terms of both mechanical, fracture and fatigue behaviour, of a specific mixture of shot-earth, that is, the shot-earth 772. In particular, an extensive experimental program is conducted, that is:

- flexural and compression tests are carried out in order to determine the flexural and compressive strengths;
- three-point bending fracture tests are carried out to analyse the fracture behaviour and to find out the elastic modulus and the fracture toughness through the Modified Two-Parameter Model (MTPM) [3,39–42];
- bending and compression cyclic tests are carried out to analyse the fatigue behaviour under flexural and compressive loading.

A home-made Finite Element (FE) numerical model [43–46] is employed to simulate the above fatigue tests, after the input data validation performed by simulating the above fracture tests.

In particular, the present paper is structured as follows. Firstly, both the mix constituents and the mixture of the shot-earth 772 are described in Section 2. The experimental program carried out is summarised in Section 3. Then, Section 4 is devoted to the input data validation and to the FE numerical model description for fatigue simulation. The numerical results obtained are discussed and compared with the corresponding experimental findings in Section 5. Finally, conclusions are summarised in Section 6.

2. Materials

The shot-earth 772 (named for simplicity "shot-earth" in the following) is a mixture composed by soil stabilised with cement, aggregates and drinking water.

2.1. Mix constituents

The soil is an excavated soil, extracted after the removal of a top-soil layer generally ranging between 25 cm and 50 cm, being such a layer characterised by a large content of organic matter. After the excavation, the soil is stockpiled and left to dry, sheltered from bad weather, without controlling temperature and relative humidity, for a few days (depending on both season and soil type). During drying, any clods are removed. Then, the soil is sieved, removing any stones, and milled.

The as-received soil is classified as a poorly graded sand with silt, according to the Unified Soil Classification System implemented in ASTM D2487-17 standard [47], with a cumulative particle-size distribution shown in Fig. 1 (see the black curve). Details may be found in Ref. [34]. The washed soil is classified as a silty sand, with a cumulative particle-size distribution shown in Fig. 1 (see the red curve).

Fig. 2. Shot-earth technique. The air stream is projected at a high velocity onto the receiving surface, representing the formwork panel.

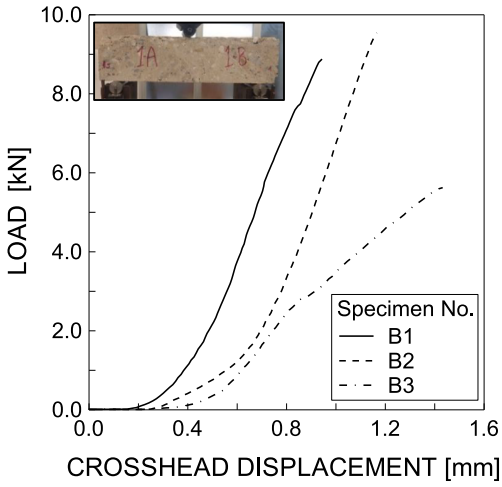

Fig. 3. Flexural testing: experimental load versus crosshead displacement.

The microstructural analysis of the soil is reported in Ref. [34], together with the chemical analysis in terms of both spectrum and chemical element concentrations.

The cement for the soil stabilisation is a CEM I 42.5 N Portland cement, complying with EN 197–1 standard [48]. Its microstructural and chemical analysis may be found in Ref. [34].

The aggregate is a commercial aggregate for concrete, made of carbonate sedimentary rocks (mainly limestone), complying with EN 12620 standard [49]. The maximum aggregate size is 8 mm.

2.2. Mixture

The shot-earth mixture is produced by introducing soil, aggregate and cement into a high-velocity air stream, in the following proportions: 7 parts of soil, 7 parts of aggregate and 2 parts of cement by volume. About 3% of water by volume is added at the spraying nozzle. The stream is projected at a high velocity onto a receiving surface, far from the nozzleman about 80–100 cm and, during impact, the material becomes compact (Fig. 2). Details may be found in Ref. [34].

The microstructural analysis of the shot-earth is reported in Ref. [34], together with the chemical analysis in terms of both spectrum, chemical concentrations and chemical element mapping.

3. Experimental program and results

The specimens employed for testing are cut from plates with sizes equal to 800mmx800mmx100mm that, after spraying, are left for curing at about 23° C of temperature and about 50% of relative humidity for about two months.

Table 1
Actual geometrical sizes of the tested specimens under three-point bending (width, d_1; depth, d_2), peak load, P_f, and flexural strength, f_{cf}.

Specimen No.	d_1 [mm]	d_2 [mm]	P_f [kN]	f_{cf} [MPa]
B1	102.35	98.80	8.87	4.00
B2	101.30	102.30	9.53	4.05
B3	101.45	100.10	5.62	2.49

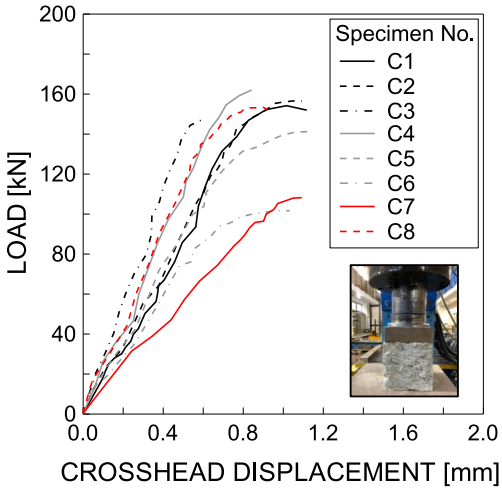

Fig. 4. Compression testing: experimental load versus crosshead displacement.

Table 2
Actual geometrical sizes of the tested specimens under compression (sides a, b, c), peak load, P_c, and compressive strength, f_c.

Specimen No.	a [mm]	b [mm]	c [mm]	P_c [kN]	f_c [MPa]
C1	96.0	100.0	95.0	154.14	16.06
C2	97.0	100.0	100.0	156.45	16.13
C3	97.0	97.0	102.0	148.01	15.73
C4	97.0	100.0	100.0	161.87	16.69
C5	98.0	99.0	102.0	141.11	14.54
C6	98.0	99.0	95.0	101.57	10.47
C7	99.0	99.0	100.0	108.03	11.02
C8	96.0	100.0	95.0	153.04	15.94

3.1. Mechanical properties testing

Both flexural and compression tests are performed.

The flexural tests are performed under three-point bending on prismatic specimens, according to UNI EN 12390–5 standard [50].

The tested specimens are characterised by nominal sizes equal to 100mm(width)x100mm(depth)x375mm(length). The nominal span is equal to 300 mm. The tests are carried out by using the universal testing machine Instron 8502 Plus, with a load cell up to 25 kN and accuracy of 0.5%. The tests are performed under load control with rate equal to 130 N/s up to failure, being the loading direction normal to the spraying one. Three tests have been carried out.

The load against crosshead displacement curves are reported in Fig. 3.

In Table 1, the actual sizes of the cross-section of each specimen are listed together with the measured value of the peak load P_f, and the computed value of the flexural strength f_{cf}. The mean value of f_{cf} is equal to 3.51 MPa, with standard deviation of ± 0.89 MPa.

The compression tests are performed on cubic specimens, according to UNI EN 12390–3 standard [51].

The tested specimens are characterised by nominal sizes equal to

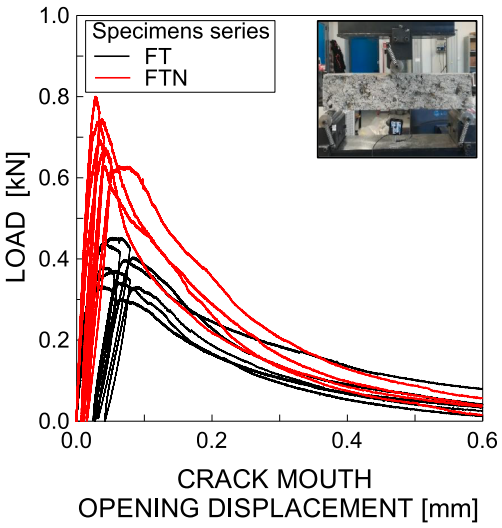

Fig. 5. Fracture toughness testing: experimental load versus Crack Mouth Opening Displacement. The curves for both specimen series FT (black lines) and FTN (red lines) are reported. (For interpretation of the references to colour in this figure legend, the reader is referred to the web version of this article.)

100mmx100mmx100mm. The tests are carried out by using a standard compression testing machine, with load cell up to 300 kN and accuracy of 1%. The tests are performed under load control with rate equal to 0.5 MPa/s up to failure, being the loading direction normal to the spraying one. Eight tests have been carried out.

The load against crosshead displacement curves are reported in Fig. 4. In Table 2, the actual sizes of each specimen are listed together with the measured value of the peak load P_c, and the computed value of the compressive strength f_c. The mean value of f_c is equal to 14.57 MPa, with standard deviation of $\pm$ 2.55 MPa.

3.2. Fracture toughness testing

The fracture toughness tests are performed on notched prismatic specimens under three-point bending, according to 50-FMC and 89-FMT RILEM recommendations [52,53], by also employing the Modified Two-Parameter Model (MTPM) [3,39–42].

The tested specimens are characterised by nominal sizes equal to 80mm(depth)x40mm(width)x375mm(length). The nominal notch length is equal to 26.7 mm (notch width lower than 1.45 mm), whereas the nominal span is equal to 320 mm.

The tests are carried out by using the universal testing machine Instron 8862, with a load cell up to 100 kN and accuracy of 0.1%. The tests are performed under Crack Mouth Opening Displacement (CMOD) control with average rate of the clip gauge equal to 0.2 mm/h, being the loading direction either coincident with or perpendicular to the spraying one. More precisely, six specimens with depth parallel to the spraying direction (FT specimen series) and six specimens with depth normal to the spraying direction (FTN specimen series) are tested.

The load against CMOD curves are reported in Fig. 5 [36–39]. It is worth noticing that, for one specimen of the FT series and for two specimens of the FTN series, no acceptable failures according to RILEM recommendations have been registered. In Table 3, the actual sizes of the cross-section and the notch length of each specimen are listed, together with the measured value of the peak load $P_{\max}$, the computed values of the elastic modulus E, and the fracture toughness $K^S_{(I+II)C}$ [36,37,39].

3.3. Fatigue testing

Both fatigue flexural tests and fatigue compression tests are performed.

The fatigue flexural tests are performed under three-point bending cyclic loading on prismatic specimens, characterised by the same nominal sizes and span as those tested under static bending [50]. The tests are carried out by using the testing machine Instron 8502 Plus, with a load cell up to 25 kN and accuracy of 0.5%. The tests are performed under load control up to failure, by applying a sinusoidal signal for the stress, with frequency of 5 Hz and fatigue ratio equal to zero, being the loading direction normal to the spraying one. It is worth noticing that, when fatigue failure does not occur within $2(10)^6$ loading cycles, the test result is referred to a run-out. The maximum value of the applied stress, $\sigma_{\max}$, normalised with respect to the average value of the flexural strength ($\bar{f}_{cf}$=3.51 MPa), is made to vary from 0.53 to 0.82. Ten tests have been carried out.

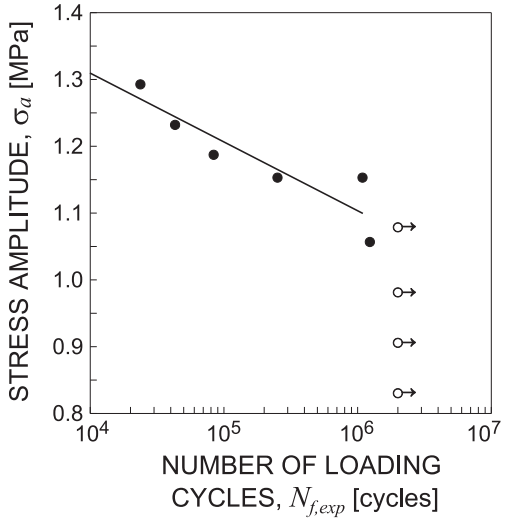

Fig. 6. Wöhler curve for pulsating bending. The symbols with arrow represent the run-outs.

Table 3
Actual geometrical sizes of the tested notched specimens under three-point bending to compute the fracture toughness (depth, W; width, B; notch length, a_0), peak load, P_{max}, elastic modulus, E, and fracture toughness, $K^S_{(I+II)C}$.

Specimen No.	W [mm]	B [mm]	a_0 [mm]	P_{max} [kN]	E [MPa]	$K^S_{(I+II)C}$ [MPa$\sqrt{\text{m}}$]
FT1	78.09	54.70	26.94	0.33	6730.78	0.18
FT2	74.36	42.02	27.34	0.45	6881.41	0.37
FT3	74.22	41.96	26.27	0.44	7164.49	0.30
FT4	78.47	43.17	26.10	0.37	6703.77	0.20
FT5	80.13	41.79	26.80	0.38	7115.65	0.25
FTN1	85.61	48.29	27.24	0.67	8321.51	0.35
FTN2	80.19	47.72	27.35	0.70	8538.66	0.32
FTN3	84.94	48.66	26.59	0.74	10877.47	0.27
FTN4	86.38	48.43	27.80	0.80	10064.61	0.39

Table 4
Actual geometrical sizes of the tested specimens under cyclic bending (width, d_1; depth, d_2), normalised loading level, $\sigma_{max}/\bar{f}_{cf}$, applied stress amplitude, σ_a, and experimental, $N_{f,exp}$, and theoretical, N_f, number of loading cycles to failure.

Specimen No.	d_1 [mm]	d_2 [mm]	$\sigma_{max}/\bar{f}_{cf}$	σ_a[MPa]	$N_{f,exp}$ [cycles]	N_f [cycles]
CB1	101.5	102.5	0.53	0.83	> 2,000,000	–
CB2	101.5	102.5	0.57	0.91	> 2,000,000	–
CB3	101.5	102.5	0.62	0.98	> 2,000,000	–
CB4	101.5	102.5	0.67	1.06	1,234,493	1,500,000
CB5	102.8	101.2	0.68	1.08	> 2,000,000	–
CB6	96.3	97.4	0.73	1.15	1,087,360	340,000
CB7	102.8	101.2	0.73	1.15	251,460	
CB8	102.7	102.2	0.75	1.19	83,800	48,000
CB9	101.5	103.2	0.78	1.23	43,100	18,000
CB10	93.5	99.2	0.82	1.29	23,715	4,400

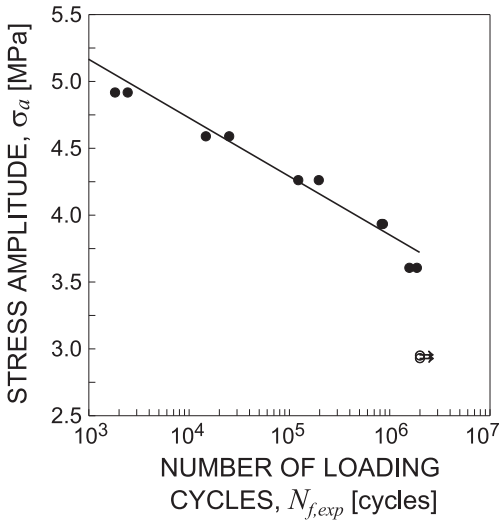

Fig. 7. Wöhler curve for pulsating compression. The symbols with arrow represent the run-outs.

The Wöhler curve for cyclic bending, determined by interpolating the fatigue results with a power function, is reported in Fig. 6, and the equation of such a curve is given by:

$$\sigma_a = 1.84493 N_{f,\exp}^{-0.03724} \quad (1)$$

being $N_{f,\exp}$ the number of loading cycles. In Table 4, the actual sizes of the cross-section of each specimen are listed together with the normalised loading level $\sigma_{\max}/\bar{f}_{cf}$, the applied stress amplitude σ_a, the experimental number of loading cycles to failure, $N_{f,\exp}$, and the theoretical one, N_f, obtained from simulation.

The fatigue compression tests are performed on cubic specimens, characterised by the same nominal sizes as those tested under static compression [51]. The tests are carried out by using an in-house-designed dynamic testing machine equipped with a 500 kN actuator and a load cell up to 1000 kN and accuracy of 1%. The tests are performed under load control up to failure, by applying a sinusoidal signal for the stress, with frequency of 5 Hz and fatigue ratio equal to zero, being the loading direction normal to the spraying one. It is worth noticing that, when the fatigue failure does not occur within $2(10)^6$ loading cycles, the test result is referred to a run-out. The maximum value of the applied stress, $\sigma_{\max}$, normalised with respect to the average value of the compressive strength ($\bar{f}_c$=14.57 MPa), is made to vary from 0.45 to 0.75. Twelve tests have been carried out.

The Wöhler curve for cyclic compression, determined by interpolating the fatigue results with a power function, is reported in Fig. 7, and the equation of such a curve is given by:

$$\sigma_a = 6.95886 N_{f,\exp}^{-0.04318} \quad (2)$$

Table 5
Actual geometrical sizes of the tested specimens under cyclic compression (sides a, b, c), normalised loading level, $\sigma_{max}/\bar{f}_c$, applied stress amplitude, σ_a, and experimental, $N_{f,exp}$, and theoretical, N_f, number of loading cycles to failure.

Specimen No.	a [mm]	b [mm]	c [mm]	$\sigma_{max}/\bar{f}_c$	σ_a[MPa]	$N_{f,exp}$ [cycles]	N_f [cycles]
CC1	100.1	99.6	100.3	0.45	2.95	> 2,000,000	–
CC2	99.8	102.4	101.2	0.45	2.95	> 2,000,000	–
CC3	98.5	100.3	102.3	0.55	3.61	1,570,900	2,000,000
CC4	101.2	99.5	100.8	0.55	3.61	1,865,317	
CC5	100.9	101.2	99.1	0.60	3.93	831,414	420,000
CC6	102.7	100.1	99.9	0.60	3.93	855,405	
CC7	98.4	100.2	101.3	0.65	4.26	122,394	65,000
CC8	100.2	101.5	99.4	0.65	4.26	196,307	
CC9	101.4	100.2	102.4	0.70	4.59	25,065	11,000
CC10	99.4	101.2	100.3	0.70	4.59	14,678	
CC11	100.6	99.6	101.2	0.75	4.92	2,439	2,100
CC12	101.6	100.1	99.7	0.75	4.92	1,826	

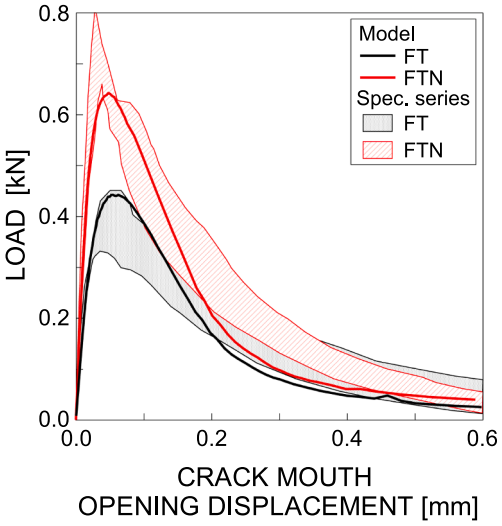

Fig. 8. Load against CMOD: comparison between experimental and numerical results (the experimental unloading/reloading branches are not represented for the sake of clarity).

being $N_{f,\exp}$ the number of loading cycles. In Table 5, the actual sizes of each specimen are listed together with the normalised loading level $\sigma_{\max}/\bar{f}_c$, the applied stress amplitude σ_a, the experimental number of loading cycles to failure, $N_{f,\exp}$, and the theoretical one, N_f, obtained from simulation.

4. Numerical simulation

A micromechanical numerical model, proposed in the past by some of the present authors [43–46] to simulate fracture and fatigue behaviour of both single phase and reinforced materials, is here employed to simulate the tests presented in **Sub-Sections 3.2 and 3.3**. Firstly, the fracture behaviour of the shot-earth 772 is modelled in order to validate the input data; then, such data are used into the model to simulate the material fatigue behaviour.

4.1. Input validation

For fracture simulation, the micromechanical model is implemented in a non-linear 2D FE home-made code in standard Fortran language, where the matrix is assumed to have a brittle behaviour, whereas the discontinuities due to the fracture process are modelled through a suitable modification of the material properties by means of a cohesive law. Further details can be found in Refs [45,54].

The notched prismatic specimens, presented in **Sub-Section 3.2**, are modelled by considering the mean geometrical sizes reported in Table 3, that is: B=44.51 mm, W=77.00 mm and a_0=27.15 mm for the FT model, and B=48.12 mm, W=83.73 mm and a_0=27.21 mm for the FTN model.

Each model requires some input data to be defined, related to the material properties:

- the Young modulus E, assumed to be equal to 6919 MPa and 9450 MPa for FT and FTN models, respectively, according to the experimental results reported in Table 3;
- the Poisson's ratio ν, assumed to be equal to 0.20 [39];
- the compressive strength f_c and the ultimate tensile strength f_t, assumed to be equal to 14.57 MPa and 3.51 MPa (that is, the mean value of the flexural strength, $\bar{f}_{cf}$), respectively, according to the experimental results reported in Tables 1 and 2;
- the energy release rate G_f, assumed to be equal to 25 N/m [39].

Table 6
Experimental values (mean value ± standard deviation) of the peak load, P_{max}, and the fracture toughness, $K^S_{(I+II)C}$, compared with the numerical ones.

Model name	P_{max} [kN]		$K^S_{(I+II)C}$ [MPa$\sqrt{\text{m}}$]	
	Experimental	Numerical	Experimental	Numerical
FT	0.40 ± 0.05	0.44	0.26 ± 0.08	0.37
FTN	0.73 ± 0.09	0.64	0.33 ± 0.05	0.42

Two mesh discretisations of 650 and 720 four-node quadrilateral plate elements are chosen for the FT and the FTN models, respectively, after convergence analyses performed on the computed stress fields.

The numerical analyses are, then, carried out by imposing a progressive vertical displacement at the top point of the central cross-section, recording both the corresponding reaction force and the CMOD.

The numerical load vs CMOD curves are plotted in Fig. 8 and compared with the experimental results in Fig. 5, that are collected into scatter bands (that is, the grey one for the FT specimen series, and the red one for the FTN specimen series).

It can be observed that a satisfactory agreement between numerical and experimental results is obtained, since the numerical curves are mostly inside the experimental scatter bands.

Moreover, the numerical results, in terms of $P_{\max}$ and $K^S_{(I+II)C}$, are compared with the average experimental ones for each model (see Table 6). It is worth noticing that the numerical fracture toughness $K^S_{(I+II)C}$ is determined by applying the MTPM to the numerical load vs CMOD curves, by using the unloading compliance C_u computed in correspondence of $P_{\max}$, and by assuming a pure Mode I crack propagation. For further details see Ref. [54].

From Table 6, it can be observed that:

- the peak load is overestimated by 11.4% from the numerical FT model, whereas it is underestimated by 12.3% from the FTN model, although the numerical peak load values are inside the experimental data ranges in both cases;
- the fracture toughness is greater than the experimental one for both FT and FTN models, even if very close to the experimental data ranges.

4.2. Fatigue simulation

For fatigue simulation, the flowchart of the micromechanical numerical model is shown in Fig. 9.

Each model, which is implemented in a home-made 2D FE code, requires the definition of the model geometry as the first step. The CB prismatic specimens and the CC cubic ones presented in **Sub-Section 3.3** are modelled by considering the mean geometrical sizes reported in Tables 4 and 5, respectively: d_1=100.56 mm and d_2=101.44 mm for the CB model, and a=100.40 mm, b=100.49 mm and c=100.66 mm for the CC model.

Other input data are the material mechanical and fatigue properties. More precisely, the mechanical properties are the same as those assumed for the FTN model presented in **Sub-Section 4.1**, that is: Young modulus equal to 9450 MPa, Poisson's ratio equal to 0.20, and compressive and ultimate tensile strengths equal to 14.57 MPa and 3.51 MPa, respectively. In addition, as far as the fatigue properties are concerned, the S-N curves obtained from both cyclic bending and compression tests, and described by **Eqs (1) and (2)**, respectively, are passed to the code as input data.

Moreover, both the loading and the boundary conditions have to be defined.

Related to the loading conditions shown in Fig. 10, the maximum number of blocks of loading cycles (together with the corresponding number of cycles) and the number of load steps need to be set. The code framework for fatigue problems can be then summarised as follows

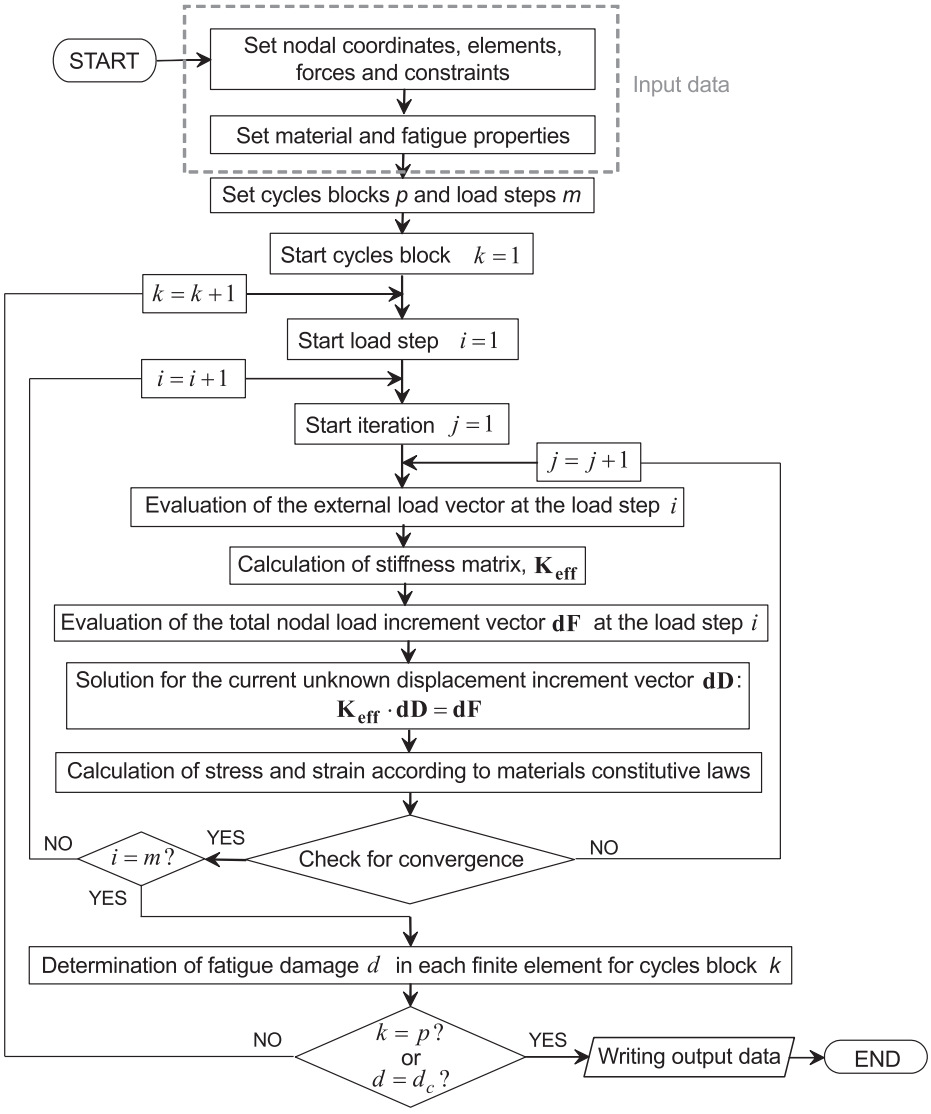

Fig. 9. Flowchart of the numerical micromechanical model for fatigue problems.

(Fig. 9):

(i) for each block of loading cycles, the load is applied by steps and, for each step, the stress and strain fields are computed according to the material constitutive law after the stiffness matrix is assembled;
(ii) the convergence conditions on the nodal displacements and the unbalanced forces are checked: if they are satisfied, next load increment follows, otherwise another iteration starts;
(iii) the iterations (i)-(ii) are repeated until the final load step is reached;
(iv) the damage parameter d is then computed in each finite element of the model;
(v) finally, the iterations (i)-(iv) are repeated until the maximum number of blocks of loading cycles or a critical value d_c of the damage parameter is achieved, whichever occurs first.

In the present simulations, the maximum number of blocks of loading cycles and the number of load steps are equal to 20 and 3, respectively. Moreover, the damage parameter d is computed by exploiting the well-known Miner linear rule for fatigue damage accumulation [55]:

$$d = \sum_{k=1}^{p} \frac{n_k}{N_k} \tag{3}$$

where p is the total number of blocks of loading cycles, whereas k is the current block. Moreover, n_k is the number of loading cycles of the k-th block, and N_k is the number of loading cycles to failure for load level and stress ratio characterising the k-th block, computed according to the material S-N curve.

The damage parameter is used in the model to update the mechanical properties of the material, such as the Young modulus, accounting for the damaging effect of cyclic loading, in accordance to the following simplified relationship:

$$E_f = E(1 - d) \tag{4}$$

where E_f is the reduced Young modulus. Note that both the damage parameter d and the reduced Young modulus E_f are computed in each FE of the mesh. If $d = 0$, no degradation of the material mechanical properties occurs (i.e. $E_f = E$), whereas the critical condition is reached when the damage parameter is equal to one (i.e. $d = d_c$=1 and $E_f \rightarrow 0$) and a condition of incipient failure is assumed.

Related to the boundary conditions, they are reported in Fig. 10, being u_x and u_y the displacements along x and y axes, respectively.

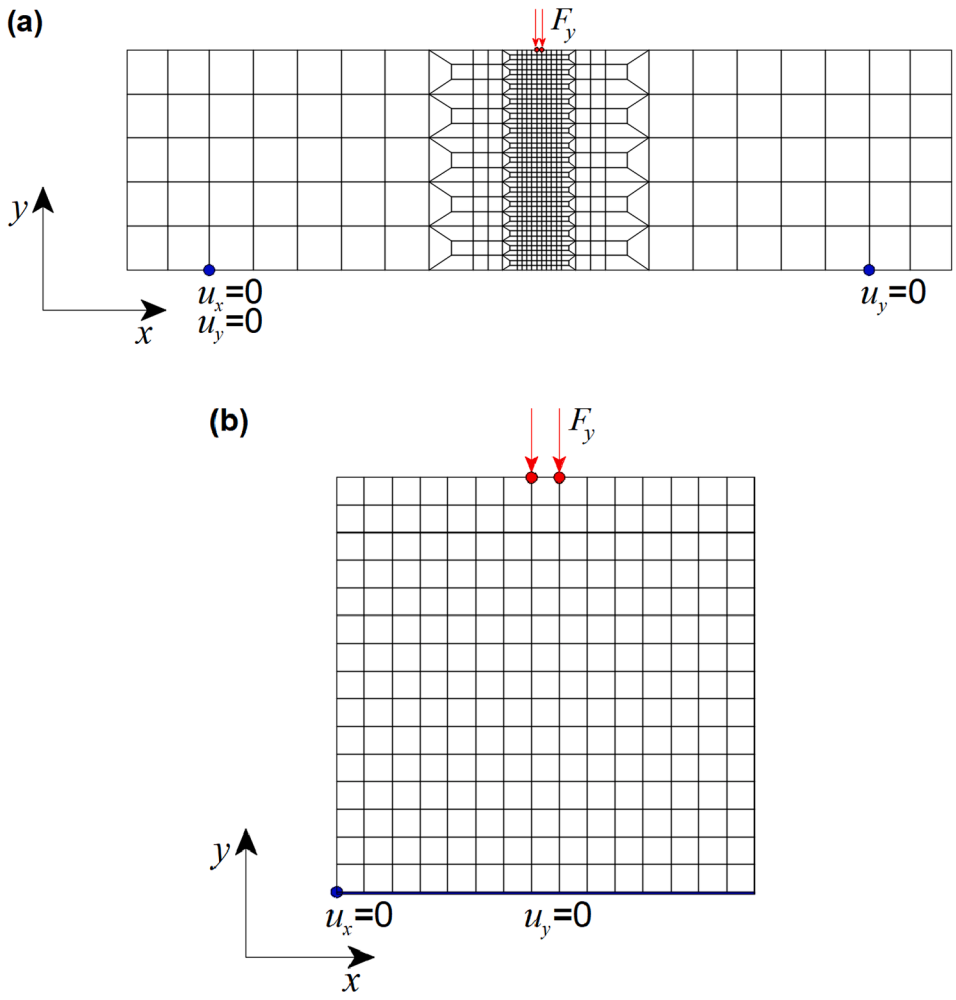

Fig. 10. Mesh discretisation for the: (a) CB model (cyclic bending loading) and (b) CC model (cyclic compression loading). The loading (in red) and the boundary conditions (in blue) are also reported. (For interpretation of the references to colour in this figure legend, the reader is referred to the web version of this article.)

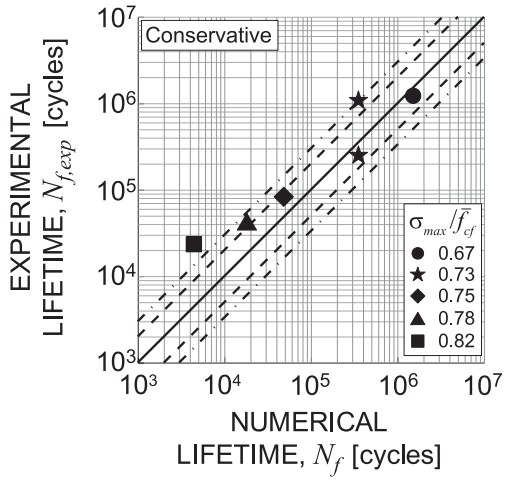

Fig. 11. Cyclic bending: comparison between the numerical, N_f, and the experimental, $N_{f,\exp}$, fatigue lifetimes.

The mesh discretisation for the CB model, obtained after a convergence analysis on the stress field, is characterised by 696 four-node quadrilateral plate elements, as is shown in Fig. 10(a), whereas the mesh discretisation for the CC model by 240 four-node quadrilateral plate elements, as is shown in Fig. 10(b).

5. Discussion

In the present Section, the numerical results related to both cyclic bending and compression are presented and discussed.

5.1. Cyclic bending

The results in terms of numerical fatigue lifetimes N_f are listed in Table 4 and compared with the experimental ones $N_{f,\exp}$ in Fig. 11, by considering only the failed specimens.

In Fig. 11, the dashed lines correspond to the scatter band with factor 2 (i.e. $N_{f,\exp}/N_f$=2 and 0.5), whereas the dash-dot lines correspond to the scatter band with factor 3 (i.e. $N_{f,\exp}/N_f$=3 and 0.33). It can be observed that 50% of results fall into the scatter band 2, whereas 83% into the scatter band 3. However, the single point falling out the scatter band 3 is on the conservative side of the graph. Moreover, the accuracy of the estimations can be evaluated by means of the root mean square error [56], T_{RMS}, which is equal to 2.58 (T_{RMS}=1.0 means that a perfect correspondence exists between experimental and estimated fatigue lifetime).

In Fig. 12, the contours of the damage parameter are shown for $\sigma_{\max}/\bar{f}_{cf}$ equal to 0.82 and four values of the number of loading cycles, that is, 1100, 2200, 3300 and 4400 cycles (for the last value, the critical damage, i.e. d_c=1, is reached in at least one element of the mesh).

As can be noticed according to the grey scale, the damage is located at the bottom of the middle cross-section, highlighted by the darker

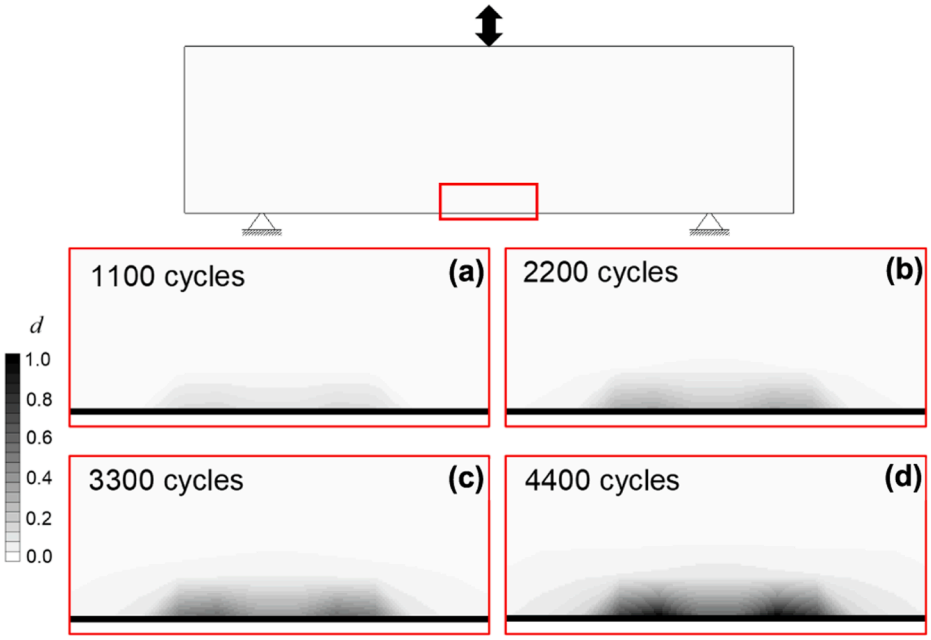

Fig. 12. Contours of the damage parameter, d, due to cyclic bending for the loading level $\sigma_{max}/\bar{f}_{cf}$=0.82, at a number of loading cycles equal to: (a) 1100, (b) 2200, (c) 3300 and (d) 4400.

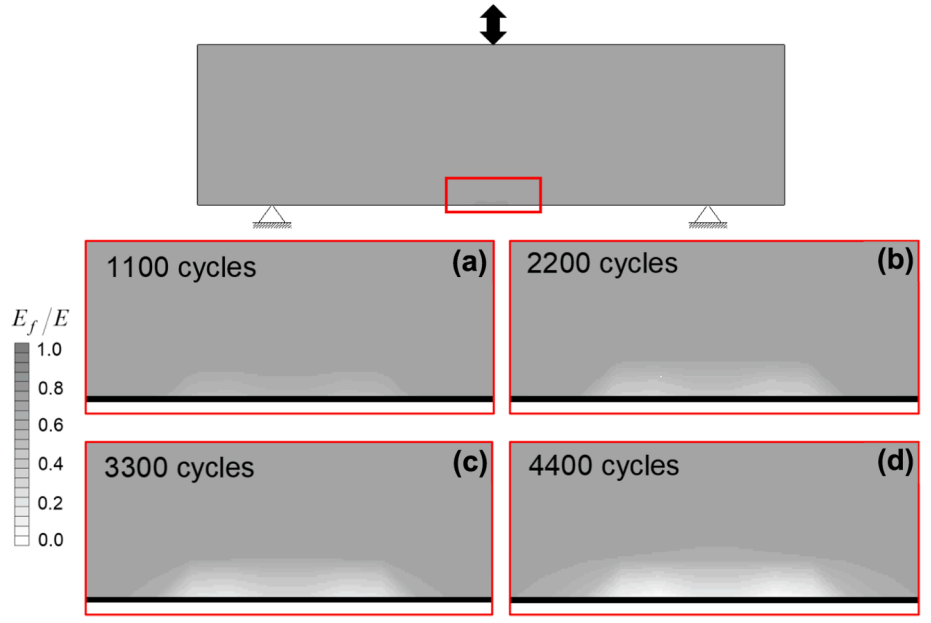

Fig. 13. Contours of the reduced Young modulus, E_f, due to cyclic bending for the loading level $\sigma_{max}/\bar{f}_{cf}$=0.82, at a number of loading cycles equal to: (a) 1100, (b) 2200, (c) 3300 and (d) 4400.

zones, as was expected, where the stress reaches its maximum value. In particular, a maximum damage value equal to 0.26 is attained after 1100 loading cycles (Fig. 12(a)), whereas maximum values equal to 0.52 and 0.78 are reached after 2200 (Fig. 12(b)) and 3300 (Fig. 12(c)) loading cycles, respectively.

In Fig. 13, the contours of the reduced Young modulus E_f, computed according to **Eq. (4)** and normalised with respect to E, are plotted for $\sigma_{\max}/\bar{f}_{cf}$ equal to 0.82 and four values of the number of loading cycles, that is, 1100, 2200, 3300 and 4400.

As is highlighted by the lighter zones in Fig. 13, the Young modulus decreases where the mesh elements are damaged. In particular, the Young modulus in such zones is reduced of about: 26.0% after 1100 loading cycles (Fig. 13(a)); 52.0% after 2200 loading cycles (Fig. 13(b)); and 78.1% after 3300 loading cycles (Fig. 13(c)). Finally, the value of E_f/E approaches zero after 4400 loading cycles in Fig. 13(d) (failure numerically predicted).

5.2. Cyclic compression

The results in terms of fatigue numerical lifetimes N_f are listed in Table 5 and compared with the experimental ones $N_{f,\exp}$ in Fig. 14, by considering only the failed specimens.

It can be observed that 60% of results fall into the scatter band 2, whereas 100% into the scatter band 3. Moreover, the accuracy of the

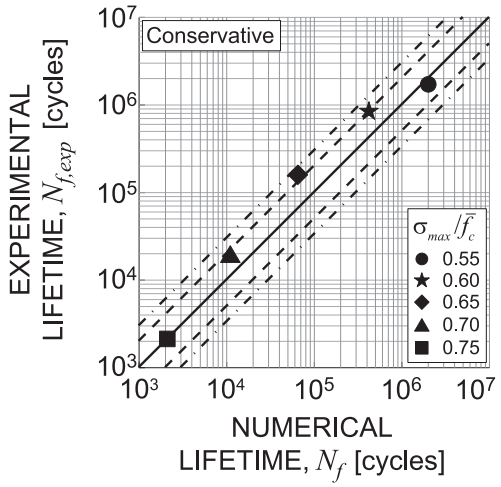

Fig. 14. Cyclic compression: comparison between the numerical, N_f, and the experimental, $N_{f,exp}$, fatigue lifetimes.

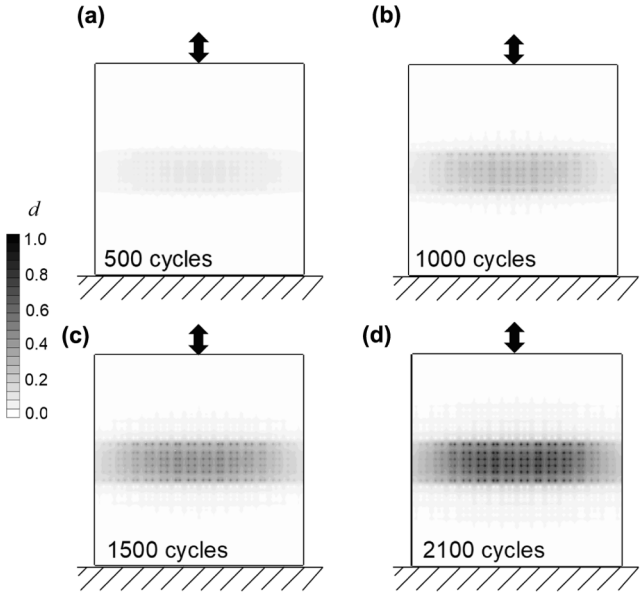

Fig. 15. Contours of the damage parameter, d, due to cyclic compression for the loading level $\sigma_{max}/\bar{f}_c$=0.75, at a number of loading cycles equal to: (a) 500, (b) 1000, (c) 1500 and (d) 2100.

estimations can be evaluated by means of the root mean square error [56], T_{RMS}, which is equal to 2.15.

In Fig. 15, the contours of the damage parameter are shown for $\sigma_{max}/\bar{f}_c$ equal to 0.75 and four values of the number of loading cycles, that is, 500, 1000, 1500 and 2100 cycles (for this last value, the critical damage, i.e. d_c=1, is reached in at least one element of the mesh).

According to the grey scale, a maximum damage value equal to 0.22 is attained after 500 loading cycles (Fig. 15(a)), whereas maximum values equal to 0.49 and 0.74 are reached after 1000 (Fig. 15(b)) and 1500 (Fig. 15(c)) loading cycles, respectively.

In Fig. 16, the contours of the reduced Young modulus E_f, computed according to **Eq. (4)** and normalised with respect to E, are plotted for $\sigma_{max}/\bar{f}_c$ equal to 0.75 and four values of the number of loading cycles, that is, 500, 1000, 1500 and 2100 cycles.

As can be noticed according to the grey scale, the Young modulus decreases where the mesh elements are damaged, as is highlighted by the lighter zones. In particular, the Young modulus in such zones is

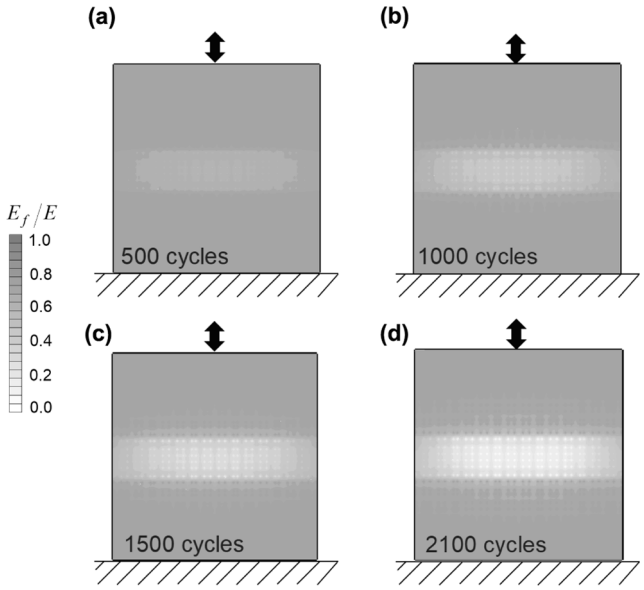

Fig. 16. Contours of the reduced Young modulus, E_f, due to cyclic compression for the loading level $\sigma_{max}/\bar{f}_c$=0.75, at a number of loading cycles equal to: (a) 500, (b) 1000, (c) 1500 and (d) 2100.

reduced of about: 22.2% after 500 loading cycles (Fig. 16(a)); 50.4% after 1000 loading cycles (Fig. 16(b)); and 74.1% after 1500 loading cycles (Fig. 16(c)). Finally, the value of E_f/E approaches zero after 2100 loading cycles in Fig. 16(d) (failure numerically predicted).

6. Conclusions

The present research work has been devoted to the mechanical, fracture and fatigue experimental characterization of the shot-earth 772, with a particular attention to its fatigue behaviour. More precisely, an extensive experimental program has been carried out, that is:

- flexural and compression tests, to determine the flexural and compressive strengths;
- three-point bending fracture tests, to analyse the fracture behaviour and to find out the elastic modulus and the fracture toughness through the Modified Two-Parameter Model;
- bending and compression cyclic tests, to analyse the fatigue behaviour under flexural and compressive loading.

A home-made FE numerical model has been used to simulate both the bending and compression cyclic tests, after the input data validation carried out by simulating the above fracture tests.

In particular, the numerical fatigue lifetimes are compared with the corresponding experimental ones, highlighting that:

- for pulsating bending, 50% of the results fall into the scatter band 2, whereas 83% into the scatter band 3, with the point outside the scatter band 3 on the conservative side of the graph. The computed root mean square error, T_{RMS}, is equal to 2.58;
- for pulsating compression, 60% of results fall into the scatter band 2, whereas 100% into the scatter band 3, with T_{RMS} equal to 2.15.

Finally, the contours of both the damage parameter and the reduced Young modulus are plotted showing the evolution of fatigue damage.

CRediT authorship contribution statement

Giovanni Pio Pucillo: Investigation, Validation, Writing – review & editing. **Andrea Carpinteri:** Funding acquisition, Writing – review &

editing. **Camilla Ronchei:** Formal analysis, Investigation, Writing – review & editing. **Daniela Scorza:** Formal analysis, Investigation, Software, Writing – original draft. **Andrea Zanichelli:** Formal analysis, Investigation, Writing – review & editing. **Sabrina Vantadori:** Conceptualization, Supervision, Funding acquisition, Writing – original draft.

Declaration of Competing Interest

The authors declare that they have no known competing financial interests or personal relationships that could have appeared to influence the work reported in this paper.

Data availability

Data will be made available on request.

Acknowledgments

The work is supported by Italian Ministry of University and Research (F.I.S.R. National Grant 2019, Project code FISR2019_00245, University of Parma Research Unit).

References

[1] Fernandes J, Peixoto M, Mateus R, Gervásio H. Life cycle analysis of environmental impacts of earthen materials in the Portuguese context: Rammed earth and compressed earth blocks. J Clean Prod 2019;241:118286.
[2] Shoji D, He Z, Zhang D, Li VC. The greening of engineered cementitious composites (ECC): A review. Constr Build Mater 2022;327:126701.
[3] Vantadori S, Carpinteri A, Guo L-P, Ronchei C, Zanichelli A. Synergy assessment of hybrid reinforcements in concrete. Compos B Eng 2018;147:197–206.
[4] Vantadori S, Carpinteri A, Zanichelli A. Lightweight construction materials: Mortar reinforced with date-palm mesh fibres. Theor Appl Fract Mech 2019;100:39–45.
[5] Li L, Wang X, Du H, Han B. Comparison of compressive fatigue performance of cementitious composites with different types of carbon nanotube. Int J Fatigue 2022;165:107178.
[6] Li L, Zheng Q, Wang X, Han B, Ou J. Modifying fatigue performance of reactive powder concrete through adding pozzolanic nanofillers. Int J Fatigue 2022;156:106681.
[7] Vantadori S, Magnani G, Mantovani L, Pontiroli D, Ronchei C, Scorza D, et al. Effect of GO nanosheets on microstructure, mechanical and fracture properties of cement composites. Constr Build Mater 2022;361:129368.
[8] Abdo A, Asker R, Atef D, Ahmed S. Experimental and numerical investigations of the flexural behaviour of Green-Ultra High Performance Fiber Reinforced Concrete beams under repeated loads. Frattura ed Integrita Strutturale 2023;17:148–70.
[9] Zhu X, Chen X, Zhang N. Experimental and numerical investigation on cyclic triaxial behavior of self-compacting concrete subjected to freeze–thaw damage. Int J Fatigue 2021;149:106277.
[10] Zhang Y, Sun Q, Xin H, Liu Y, Correia JA, Berto F. Probabilistic flexural fatigue strength of ultra-lightweight cement concrete and high strength lightweight aggregate concrete. Int. J. Fatigue 2022;158:106743.
[11] Ho LS, Huynh T-P. Long-term mechanical properties and durability of high-strength concrete containing high-volume local fly ash as a partial cement substitution. Results Eng. 2023;18:101113.
[12] Li C, Li J, Ren Q, Zheng Q, Jiang Z. Durability of concrete coupled with life cycle assessment: Review and perspective. Cem Concr Compos 2023;139:105041.
[13] Xue G, Zhu H, Xu S, Dong W. Fatigue performance and fatigue equation of crumb rubber concrete under freeze–thaw cycles. Int J Fatigue 2023;168:107456.
[14] Brinkmann M, Wiehle P. Correlation between relative humidity and the strength and deformation characteristics of unstabilised earth masonry. Constr Build Mater 2023;366:130048.
[15] Williamson JA, Rutz FR. Earth construction: Poured earth mix design. In: Rammed Earth Construction. CRC Press; 2015. p. 177–80.
[16] Rincón L, Carrobé A, Martorell I, Medrano M. Improving thermal comfort of earthen dwellings in sub-Saharan Africa with passive design. J Build Eng 2019;24:100732.
[17] Cuitiño-Rosales MG, Esteves-Miramont A, Najar LE. Response of wattle and daub walls to condensation problems. Habitat Sustentable 2022;12(2):84–97.
[18] Thompson D, Augarde C, Osorio JP. A review of current construction guidelines to inform the design of rammed earth houses in seismically active zones. J Build Eng 2022;54:104666.
[19] Boussaa N, Kheloui F, Chelouah N. Mechanical, thermal and durability investigation of compressed earth bricks stabilized with wood biomass ash. Constr Build Mater 2023;364:129874.
[20] Bredenoord J, Kulshreshtha Y. Compressed Stabilized Earthen Blocks and Their Use in Low-Cost Social Housing. Sustainability 2023;15:5295.
[21] Guettatfi L, Hamouine A, Himouri K, Labbaci B. Mechanical and Water Durability Properties of Adobes Stabilized with White Cement, Quicklime and Date Palm Fibers. Int J Architectural Heritage 2023;17(4):677–91.
[22] Koutous A, Hilali E. Compression stress-strain curve of rammed earth: Measuring and modelling. Results Eng 2023;18:101012.
[23] Touati K, Le Guern M, El Mendili Y, Azil A, Streiff F, Carfrae J, et al. Earthen-based building: In-situ drying kinetics and shrinkage. Constr Build Mater 2023;369:130544.
[24] Koci P, Foster CD. A fiber-reinforced constitutive model for earthen materials. Acta Geotech 2023;18:279–98.
[25] Han W, Wu F, Cheng Y, Wang H, Chu S. Compressive performance of adobe masonry strengthened with glass-fiber reinforced matrix composites. Mater Struct 2023;56:53.
[26] Kaluder J, Kraus I, Perić A, Kraus L. Shear Strength of Reproduced Soil Mixtures Based on Samples from Rammed Earth Walls from Eastern Croatia. Appl Sci 2022;12:11708.
[27] Miccoli L, Müller U, Fontana P. Mechanical behaviour of earthen materials: A comparison between earth block masonry, rammed earth and cob. Constr Build Mater 2014;61:327–39.
[28] Arto I, Gallego R, Cifuentes H, Puertas E, Gutiérrez-Carrillo ML. Fracture behavior of rammed earth in historic buildings. Constr Build Mater 2021;289:123167.
[29] Hussaini SMS, Toufigh V. Strength and Fracture Behaviour of Rammed-Earth Materials. J Mater Civ Eng Online 2019;31:10.
[30] Aymerich F, Fenu L, Francesconi L, Meloni P. Fracture behaviour of a fibre reinforced earthen material under static and impact flexural loading. Constr Build Mater 2016;109:109–19.
[31] Hračov S, Pospíšil S, Garofano A, Urushadze S. In-plane cyclic behaviour of unfired clay and earth brick walls in both unstrengthened and strengthened conditions. Mater Struct 2016;49:3293–308.
[32] Arslan ME, Emiroğlu M, Yalama A. Structural behavior of rammed earth walls under lateral cyclic loading: A comparative experimental study. Constr Build Mater 2017;133:433–42.
[33] Yang X, Wang H, Zhao Z. Cyclic Behavior of Confined Cement-Stabilized Rammed Earth Walls. Shock Vib 2018. 2983052.
[34] Vantadori S, Żak A, Sadowski Ł, Ronchei C, Scorza D, Zanichelli A, et al. Microstructural, chemical and physical characterisation of the Shot-Earth 772. Constr Build Mater 2022;341:127766.
[35] Vantadori S, Colpo A, Friedrich L, Iturrioz I. Numerical simulation of the shear strength of the shot-earth 772-granite interface. Constr Build Mater 2023;363:129450.
[36] Vantadori S, Ronchei C, Scorza D, Zanichelli A, Carpinteri A. Fracture toughness of the shot-earth 772. Procedia Struct Integrity 2022;42:133–8.
[37] Zanichelli A, Vantadori S, Ronchei C, Scorza D. Numerical simulation of fracture behaviour of the shot-earth 772. Procedia Struct Integrity 2022;42:118–24.
[38] Colpo A, Vantadori S, Friedrich L, Zanichelli A, Ronchei C, Scorza D, et al. A novel LDEM formulation with crack frictional sliding to estimate fracture and flexural behaviour of the shot-earth 772. Compos Struct 2023;305:116514.
[39] Vantadori S, Ronchei C, Scorza D, Zanichelli A. Experimental tests and FE simulations to compute the mechanical and fracture properties of the shot-earth 772. Fatigue Fract Eng Mater Struct 2023;46(1):49–62.
[40] Vantadori S, Carpinteri A, Fortese G, Ronchei C, Scorza D. Mode I fracture toughness of fibre-reinforced concrete by means of a modified version of the two-parameter model. Procedia Struct Integrity 2016;2:2889–95.
[41] Carpinteri A, Fortese G, Ronchei C, Scorza D, Vantadori S. Mode I fracture toughness of fibre reinforced concrete. Theor Appl Fract Mech 2017;91:66–75.
[42] Scorza D, Luciano R, Mousa S, Vantadori S. Fracture behaviour of hybrid fibre-reinforced roller-compacted concrete used in pavements. Constr Build Mater 2021;271:121554.
[43] Brighenti R, Scorza D. Numerical modelling of the fracture behaviour of brittle materials reinforced with unidirectional or randomly distributed fibres. Mech Mater 2012;52:12–27.
[44] Brighenti R, Scorza D. A micro-mechanical model for statistically unidirectional and randomly distributed fibre-reinforced solids. Math Mech Solids 2012;17(8):876–93.
[45] Scorza D. Mechanical Modelling of Short-Fibre-Reinforced Materials under Static or Cyclic Loading, PhD Thesis, 2015, ISBN: 978-88-31482-00-4.
[46] Brighenti R, Carpinteri A, Scorza D. Micromechanical crack growth-based fatigue damage in fibrous composites. Int J Fatigue 2016;82:98–109.
[47] D2487 – 17 ASTM standard. Standard Practice for Classification of Soils for Engineering Purposes (Unified Soil Classification System).
[48] EN 197-1:2011 standard. Cement - Part 1: Composition, specifications and conformity criteria for common cements.
[49] EN 12620:2002+A1:2008 standard. Aggregates for concrete.
[50] UNI EN 12390-5:2019 Prove sul calcestruzzo indurito - Parte 5: Resistenza a flessione dei provini.
[51] UNI EN 12390-3:2019 Prove sul calcestruzzo indurito - Parte 3: Resistenza alla compressione dei provini.
[52] RILEM Technical Committee, 50-FMC. Determination of the fracture energy of mortar and concrete by means of three-point bend test on notched beams, proposed RILEM draft recommendations. Mater Struct. 1985; 18: 285-290.
[53] RILEM Technical Committee, 89-FMT. Determination of fracture parameters (KsIC and CTODc) of plain concrete using three-point bend tests, proposed RILEM draft recommendations. Mater Struct. 1990; 23: 457-460.

[54] Scorza D, Ronchei C, Vantadori S, Zanichelli A. Size-effect independence of hybrid fiber-reinforced roller-compacted concrete fracture toughness. Compos Part C: Open Access 2022;9:100306.
[55] Miner MA. Cumulative Damage in Fatigue. J Appl Mech 1945;3:159–64.
[56] Vantadori S, Carpinteri A, Fortese G, Ronchei C, Scorza D, Zanichelli A. Fatigue lifetime evaluation of notched components: Implementation of the control volume concept in a strain-based LCF criterion. Theor Appl Fract Mech 2018;97:400–8.